

A Multi-Epoch *HST* Study of the Herbig-Haro Flow from XZ Tauri

John E. Krist¹, Karl R. Stapelfeldt¹,
 J. Jeff Hester², Kevin Healy²,
 Steven J. Dwyer³, and
 Carl L. Gardner⁴

ABSTRACT

We present nine epochs of *Hubble Space Telescope* optical imaging of the bipolar outflow from the pre-main sequence binary XZ Tauri. Our data monitors the system from 1995 – 2005 and includes emission line images of the flow. The northern lobe appears to be a succession of bubbles, the outermost of which expanded ballistically from 1995 – 1999 but in 2000 began to deform and decelerate along its forward edge. It reached an extent of 6'' from the binary in 2005. A larger and fainter southern counterbubble was detected for the first time in deep ACS images from 2004. Traces of shocked emission are seen as far as 20'' south of the binary. The bubble emission nebulosity has a low excitation overall, as traced by the [S II]/H α line ratio, requiring a nearly comoving surrounding medium that has been accelerated by previous ejections or stellar winds.

Within the broad bubbles there are compact emission knots whose alignments and proper motions indicate that collimated jets are ejected from each binary component. The jet from the southern component, XZ Tau A, is aligned with the outflow axis of the bubbles and has tangential knot velocities of 70 – 200 km s⁻¹. Knots in the northern flow are seen to slow and brighten as they approach the forward edge of the outermost bubble. The knots in the jet from the other star, XZ Tau B, have lower velocities of \sim 100 km s⁻¹.

To explain the observations of the outer bubble, we propose that the XZ Tau A stellar jet underwent a large velocity pulse circa 1980. This ejection quickly overtook older, slower-moving ejecta very near the star, producing a \sim 70 km s⁻¹ shock in a hot (T \sim 80,000 K), compact “fireball”. The initial thermal pressure of this gas parcel drove

¹Jet Propulsion Laboratory, California Institute of Technology, 4800 Oak Grove Drive, Pasadena CA 91109 USA

²Arizona State University, School of Earth and Space Exploration, Tempe, AZ 85287-1404

³649 E. Ridgecrest Blvd., Ridgecrest CA 93555

⁴Arizona State University, Dept. of Mathematics and Statistics, Tempe, AZ 85287-1804

the expansion of a spherical bubble. Subsequent cooling caused the bubble to transition to ballistic expansion, followed by slowing of its forward edge by mass-loading from the pre-shock medium. Repeated pulses may explain the multiple bubbles seen in the data. Collimated jets continue to flow through the bubble’s interior, and with the fading of the original fireball they are becoming the primary energizing mechanism for the emission line structures. Future evolution of the flow should see the outer bubble structures fade from view, and the emergence of a more typical Herbig-Haro jet/bowshock morphology. We present a preliminary numerical model of a pulsed jet to illustrate this scenario.

Subject headings: binaries: general – Herbig-Haro Objects — stars: individual (XZ Tau) — stars: pre-main sequence

1. Introduction

XZ Tauri (HBC 50, Haro 6-15) is a pre-main sequence binary system located in the L1551 molecular cloud at a distance of 140 pc. Both components of the $0''.3$ binary have strong emission lines that are characteristic of classical T Tauri stars (Hartigan & Kenyon 2003; White & Ghez 2001). These studies have determined spectral types of M3-M3.5 for the southern component and M1.5-M2 for the northern one. The spectrum of the S component in our data (hereafter XZ Tau A) indicates that it is a typical T Tauri star, while the N component (XZ Tau B) has large amount of spectral veiling and numerous emission lines, especially Ca II (Hartigan & Kenyon 2003). The relative brightnesses of the two components fluctuates at optical wavelengths, with the S component 1–2 mags brighter in 1995 and 1997 *Hubble Space Telescope* (*HST*) images (Krist et al. 1997; White & Ghez 2001) and the N component brighter in 1996 and 2000 (White & Ghez 2001; Hartigan & Kenyon 2003). The XZ Tau system is an X-ray source with strong variability and a hard spectrum (Carkner et al. 1996; König et al. 2001; Giardino et al. 2006). It is also a 3.6 cm radio continuum source (Rodriguez et al. 1994).

XZ Tau was identified by Mundt et al. (1990) as the source of a bipolar, collimated outflow (HH 152) along a position angle of $\sim 15^\circ$ with radial velocities of up to $\sim 80 \text{ km s}^{-1}$, and the blueshifted lobe to the N. Welch et al. (2000) found an expanding shell of ^{13}CO emission ~ 0.1 pc across and centered on XZ Tau, which may be related to this outflow. Krist et al. (1997, 1999) resolved the inner parts of the outflow using PSF-subtracted *HST* images, finding an unusual bubble of emission nebulosity within $5''$ of the star. Marked changes were seen in this bubble over 1995 – 1998: the onset of limb brightening, the dissipation of a bright knot within the bubble, and large outward proper motions ($\sim 150 \text{ km s}^{-1}$) indicative of a dynamical age of only 20 years. However, they were unable to determine if the bubble energetics were dominated by the energy of an initial blast or the ongoing input of energy from a continuous jet.

To measure flow accelerations and monitor the growth and decay of emission knots, multiple epochs and high spatial resolution are needed. *HST* is a particularly valuable tool for the study

of Herbig-Haro flows such as XZ Tau’s. For sources at 140 pc distance, its $\sim 0''.05$ resolution corresponds to linear scales of 10^{12} m, small enough to resolve the cooling zones of radiative shocks. This resolution is also sufficient to measure proper motions of ~ 100 km s $^{-1}$ on temporal baselines of only one year.

We report here the results of an imaging campaign spanning 1995 – 2005 that monitored the evolution of the XZ Tau outflow. The new data include emission line images that reveal the excitation structure of the XZ Tau bubble, and deeper, wider-field images taken with the *HST* Advanced Camera for Surveys (ACS). Some of our data has also been discussed by Coffey et al. (2004).

2. Observations

Our monitoring campaign consisted of deep *HST* imaging of the XZ Tau field at multiple epochs over 1995 – 2004, with an additional observation serendipitously obtained in another program in 2005 (Table 1). The images were taken using the Wide Field and Planetary Camera 2 (WFPC2) and the ACS. Most of these also include the young stars HL Tauri (Stapelfeldt et al. 1995), HH 30 (Burrows et al. 1996; Watson & Stapelfeldt 2007), and LkH α 358. The entire 2004 ACS F625W field is shown in Figure 1 with the XZ Tau stellar components subtracted as described later. Approximately $3.5'$ on a side, the field includes the jet and edge-on disk of HH 30, the jet and envelope of the obscured star HL Tau, and the nebulous star LkH α 358. Reflection nebulosity fills much of the field. The smaller WFPC2 fields, $\sim 2.6'$ on a side, cover the central portion of this frame. Except for the XZ Tau bubble and HH 30 outflows, it is difficult to distinguish reflection and emission nebulosity in this broadband image. A color version of a portion of this field using the ACS FR656N and F658N images is shown in Figure 2, highlighting the emission nebulosities.

Eight epochs of images from 1995 – 2002 were obtained with WFPC2. Seven of these were sensitive enough to detect XZ Tau outflow structures. The WFPC2 Planetary Camera (PC1; $0''.0455$ per pixel) was used for all of these observations except December 1998, when the WFPC2 Wide Field Camera channel 2 (WF2; $0''.0997$ per pixel) was used. F675W (WFPC2 *R* band) images were taken at all of these epochs. This filter’s bandpass includes several nebular emission lines, including H α , [S II], [N II], and [O I]. F814W (WFPC2 *I* band) images, which are devoid of significant emission lines, were taken in 1995, 1999, and 2000 to search for circumstellar or circumbinary disks in reflected light, though none were detected. The four observations during 1999 – 2002 also included exposures in the F656N (H α) and F673N ([S II]) narrowband filters. The 1998 – 2002 PC1 sequences comprised both deep integrations and short, unsaturated exposures to allow measurements of the positions and fluxes of the binary components. The 1998 WF2 observations included F439W (WFPC2 *B* band) and deep F675W images (Figure 3). A defocused ghost image of the binary is seen in the WF2 F675W image $8''$ NE of the stars near the axis of the bubble.

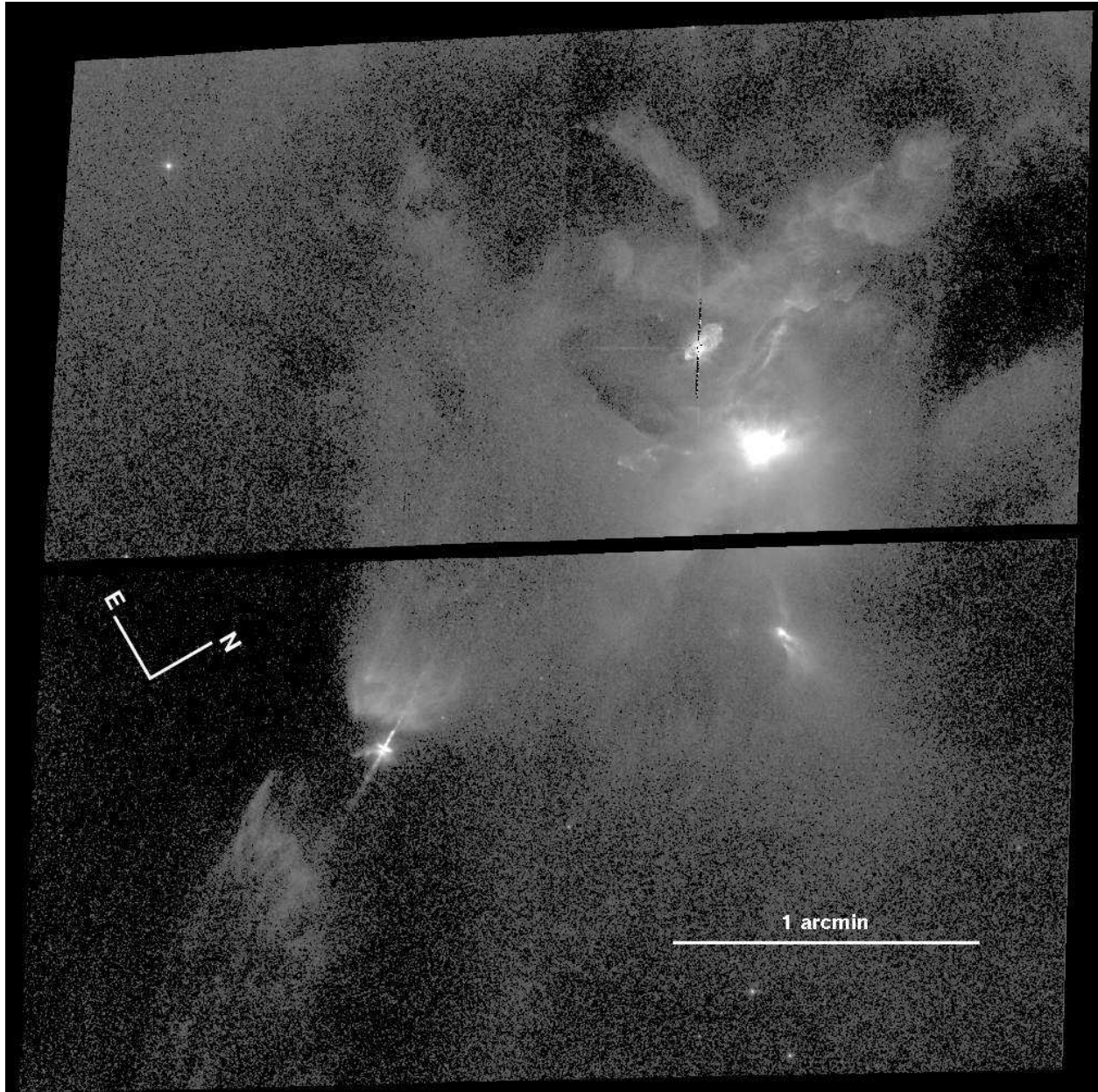


Fig. 1.— *ACS R* band image of the XZ Tau/HL Tau/HH 30 field, displayed to emphasize faint nebulosity. The HH 30 disk and bipolar jet are seen in the lower left quadrant, with nearby large-scale reflection nebulosity. LKH α 358 is the nebulous object in the lower right quadrant. XZ Tau and its bubbles can be seen in the upper right quadrant with an overexposed and nebulous HL Tau located to its west.

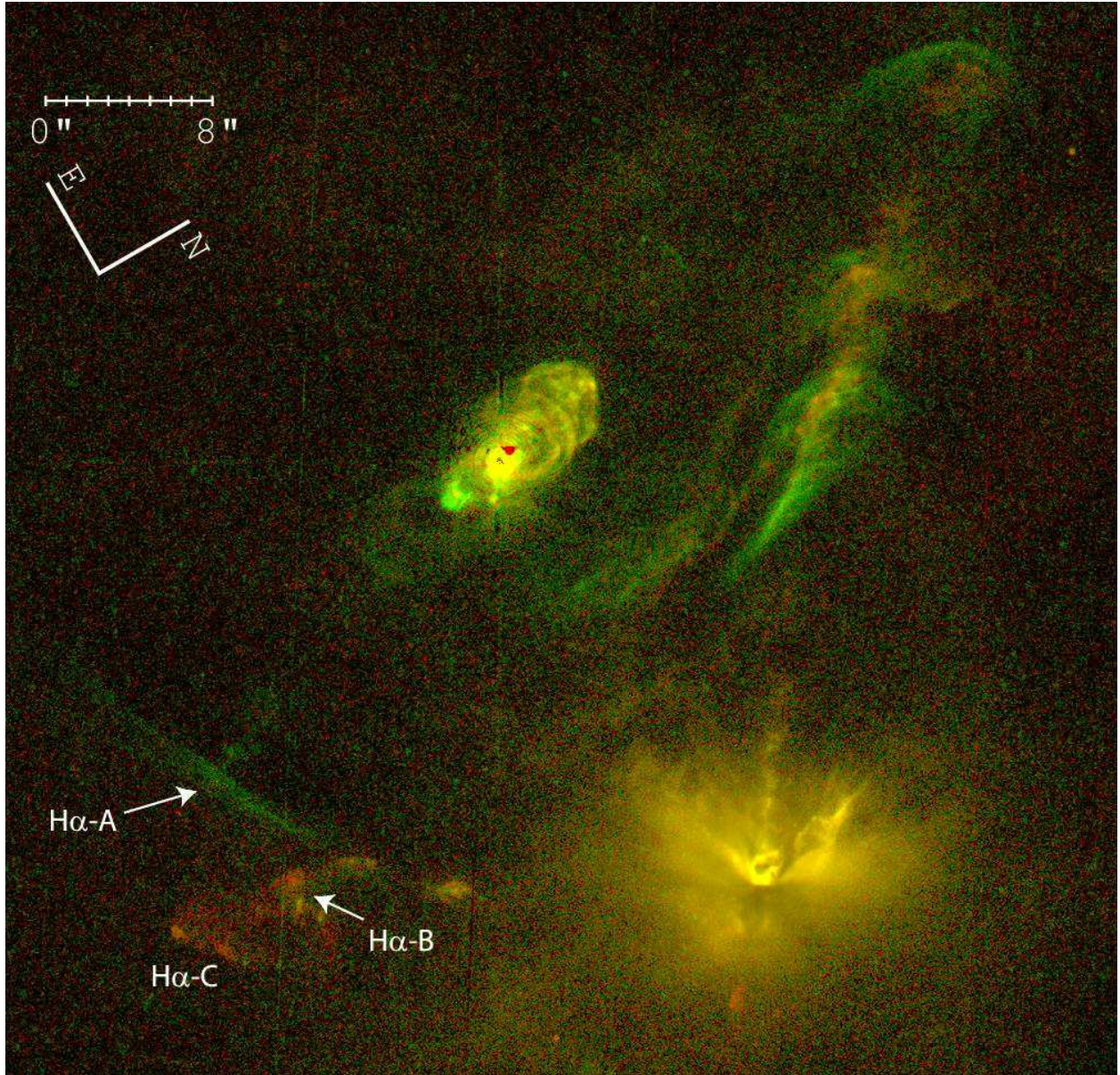


Fig. 2.— 2004 color *ACS* image of the XZ Tau / HL Tau field. The F658N filter image ($H\alpha + [N\ II]$) is shown in the green channel, and the FR656N filter image ($[S\ II]$) is shown in the red channel. The region containing the compact nebulosity surrounding HL Tau (lower right) has been reduced in intensity relative to Figure 1 in order to bring it within the dynamic range of the rest of the image. $H\alpha$ -B and $H\alpha$ -C are collectively known as HH 153.

The 2004 and 2005 images were taken using the ACS Wide Field Camera (WFC; $\sim 0''.05$ per pixel). The WFC provides a significant improvement over WFPC2. It has 3–4 times more throughput than WFPC2 in the R band, covers a larger area, and has lower read noise. It also lacks the backscatter created by the matte surface of the WFPC2 CCDs that creates an additional halo of scattered light around stars. As a newer camera, it also has no significant trailing artifacts caused by reduced charge transfer efficiency from radiation damage that increases the background noise in WFPC2 due to trailing of cosmic rays.

The ACS WFC images from 2004 were taken through filters F625W (Sloan r), F658N ($H\alpha$ and [N II]), and FR656N, which is a ramp filter that was positioned to provide [S II] line imaging at $\lambda = 6730 \text{ \AA}$. The FR656N filter has a reduced field that limited imaging to the region close XZ Tau, including HL Tau but not HH 30 or LkH α 358. The F625W filter bandpass includes the same emission lines as WFPC2 F675W. Short and long exposures were taken in each filter to provide combined, high-dynamic-range images. To provide a reference point spread function (PSF) for subtraction of the XZ Tau stars, separate observations were also made of HD 225213, an isolated M1V star ($V=8.57$). Short (0.5 s) and medium (40 s, 50 s, and 75 s in F625W, F658N, and FR656N, respectively) exposures in each filter were taken of this star, providing comparable signal levels to the XZ Tau images. The star was saturated in the short exposures (0.5 s is the shortest exposure possible with the WFC).

The 2005 ACS WFC images were taken through 0° , 60° , and 120° polarizers with filter F606W (ACS wide V), which contains the same emission lines as ACS F625W and WFPC2 F675W. These were part of *HST* program 10178 that studied the polarization of nearby HL Tau. Exposures of 536 s each were taken in each polarizer. Unsaturated images of the stars at this epoch were not available. The polarizers have a limited field of view, so HH 30 was not visible. No reference PSF star images were obtained at this epoch.

The WFPC2 and ACS images were calibrated (bias and dark subtraction, flat fielding) by the *HST* pipeline. Duplicate exposures were combined using cosmic ray rejection. When available, scaled data from short exposures replaced saturated pixels in longer ones. Because WFPC2 has a small amount of geometric distortion across its field, after PSF subtraction the images were remapped using cubic convolution interpolation and the distortion solutions provided by the Space Telescope Science Institute. ACS has significantly more distortion than WFPC2, and its PSF-subtracted images were likewise corrected. Distortion corrections were applied after subtraction to reduce the number of interpolations (the target and reference PSFs were taken at similar field positions).

The ACS polarizers introduce an additional amount of distortion. Our analyses of normal and polarized ACS images of the same star field corrected for distortion by the *HST* pipeline indicated that the current distortion solutions for the polarizers result in 2 – 3 pixel errors across the field. These solutions were derived from pre-launch calibrations and have not been verified with on-orbit data until now (polarizers are usually used with the smaller-field High Resolution Camera and

rarely with the WFC). We produced a refined solution for each polarizer by fitting polynomials to the positions of ~ 1000 stars measured in the uncorrected-polarized and corrected-nonpolarized star field images. The new solution reduces the maximum errors, when compared to the unpolarized image, to < 0.4 pixel across the field. This distortion solution is available from the author.

As we are interested in intensity rather than polarization, the polarized images were combined. The 60° and 120° polarizer images were shifted by subpixel amounts to align them with the 0° image, and the three registered images were then added together to form an intensity image using the weights described in the ACS Data Handbook (Pavlovsky et al. 2006). Because the distortion for each polarizer is different, the separate images needed to be undistorted prior to combining and PSF subtraction.

3. Results

3.1. Measurements and Subtractions of the XZ Tau Stars

The mean surface brightness of the XZ Tau nebula within $2'' - 3''$ of the stars is comparable to that of the wings of the stellar PSFs in the R band images. In these broadband filters, the line emission from the nebula must compete with the continuum flux in the wings of the PSFs. In the narrowband filters the contrast is more favorable. The PSF wings can be greatly reduced to improve the contrast by subtracting an image of another point source that is registered in position and scaled in intensity to the target. Because of diffraction and scattering effects, the fine structure in the PSF is wavelength-dependent and is sensitive to the color of the star over a broad passband. The best subtractions are achieved using a reference star image of similar color as the target. In WFPC2, the high-spatial-frequency PSF structure also varies depending on the position of the object in the field of view. Mismatches between PSFs caused by positional differences can create significant subtraction residuals. ACS PSFs are largely position-independent, except in the core where field-dependent focus, coma, and astigmatism effects are seen over large field angles. The *HST* PSF also varies slightly in focus over an orbit due to thermal effects.

In the WFPC2 PC1 images, XZ Tau was observed near the edge of the field, and a review of data in the *HST* archive did not provide any suitably exposed reference PSF stars near the same location in the filters used. The only available alternative was to use simulated PSFs produced by the Tiny Tim software package (Krist & Hook 1997). While such PSFs can be generated for a given object color and position on the detector, they do not fully reproduce the details in the wings, resulting in some significant subtraction residuals. They can, however, match quite well in the core given an accurate set of optical aberration parameters, and they can be created on subsampled grids that enable improved registration to the observed stars. They are thus useful for PSF fitting photometry, especially of close binaries like XZ Tau.

As in our previous analysis of the 1998 XZ Tau image, phase retrieval (Krist & Burrows 1995)

Table 1. List of Exposures

Date	Filter	Exposures	<i>HST</i> Program
1995 Jan 05	F675W	2x400 s	GTO 5768
	F814W	2x600 s	(Krist et al. 1997)
1997 Mar 08	F656N	2x20 s	GO 6735
	F675W	2x3.5 s	(White & Ghez 2001)
	F814W	2x1.8 s	
1998 Mar 06	F675W	2x1200 s	GTO 6855 (Krist et al. 1999)
1998 Dec 01	F439W	2x1200 s	GO 6754
	F675W	4x1200 s	(this work)
1999 Feb 03	F656N	120 s, 2x1000 s	GO 8289
	F673N	180 s, 2x1000 s	(this work)
	F675W	6 s, 2x1000 s	
	F814W	6 s, 2x1000 s	
2000 Feb 06	F656N	120 s, 2x1000 s	GO 8289
	F673N	180 s, 2x1000 s	(this work)
	F675W	2x6 s, 923 s, 1000 s	
	F814W	6 s, 2x1000 s	
2001 Feb 10	F656N	120 s, 2x1000 s	GO 8771
	F673N	180 s, 2x1000 s	(this work)
	F675W	2x6 s, 2x1000 s	
2002 Feb 12	F656N	120 s, 2x1000 s	GO 9236
	F673N	180 s, 2x1000 s	(this work)
	F675W	2x6 s, 2x1000 s	
2004 Jan 20	F625W	2 s, 2x1228 s	GO 9863
	FR656N	20 s, 2x1200 s	(this work)
	F658N	15 s, 2x1164 s	
2005 Jan 4	F606W + 0° pol	2x268 s	GO 10178
	F606W + 60° pol	2x268 s	(this work)
	F606W + 120° pol	2x268 s	

was used to measure the aberrations appropriate for each image to produce the most accurate Tiny Tim models. This process is essentially fitting PSF models to the observed image while iteratively adjusting the aberration parameters (defocus, coma, astigmatism) until an optimal match is achieved. The brighter star in each image was fitted while the fainter one was masked. The derived aberrations were then entered into Tiny Tim. Object spectra were chosen that matched the reported types and extinctions. The models were then generated on grids subsampled by a factor of five along each axis.

The binary components in each filter at each epoch were simultaneously fitted using the model PSFs. At each iteration of this nonlinear least squares optimization process the position of each star’s PSF was adjusted by a subpixel amount using cubic convolution interpolation and its intensity updated. The resulting subsampled, synthetic image of the binary was rebinned to normal pixel scaling and convolved with a kernel that reproduces blurring caused by CCD charge diffusion. This process not only provides photometry and astrometry of the binary but also creates a synthetic image of the binary that can be subtracted from the observed data.

The 1995 WFPC2 F675W PC1, 1998 WFPC2 WF2, and 2005 ACS images of XZ Tau and the 2004 ACS images of HD 225213 were not fit in this manner because the stars were saturated. The 1995 measurements were derived using the procedures discussed by Krist et al. (1997). The 1998 WF2 star images were merged due to the lower resolution combined with saturation, so no attempts were made to derive photometric or astrometric values, nor were PSF subtractions performed. For the 2005 ACS images of XZ Tau, Tiny Tim PSFs were manually shifted and normalized until the stars appeared properly subtracted. Because of the limitations of this procedure, it is assumed that the flux and position measurements are significantly worse than for the other epochs, and so the data from this epoch are best used to determine morphological changes. Also, the combination of the polarizers and a different filter (F606W versus F625W or F675W) further increases the possible quantitative errors introduced by these measurements.

Because the 2004 image of HD 225213 was saturated in the shortest exposure, its photometry was derived by first multiplying the saturated pixels by the number of electrons per full CCD well for that detector location (Gilliland 2004). We then directly computed the flux within a 1” radius of the star, which fully encompassed the saturated region. This flux was then corrected by dividing it by the known fraction of PSF flux within the aperture to derive the total stellar flux. The measured flux was used to normalized the star image relative to the XZ Tau stars prior to PSF subtraction.

The derived XZ Tau stellar brightnesses are given in Table 2. The broadband fluxes were converted to standard R and I_c magnitudes using the SYNPHOT synthetic photometry program with input spectra of similar spectral type and extinction as reported for the binary components. Following the method described by White & Ghez (2001), the stellar fluxes in the narrowband filters were converted to equivalent widths (EWs). The photospheric contribution in each line filter was estimated by computing the mean *narrowband*/ R flux ratio using SYNPHOT with input spectra from a number of stars with similar spectral types and no known emission (from the

BPGS catalog included with SYNPHOT). The measured R band flux of each XZ Tau star was multiplied by this ratio and then subtracted from its measured narrowband flux. The effective rectangular width of each filter, RW_{filter} was determined from a SYNPHOT-produced throughput curve; these widths are 28.5Å (WFPC2 F656N), 63.3Å (WFPC2 F673N), 71.9Å (ACS F658N), and 132.4Å (ACS FR656N centered at $\lambda=6730\text{\AA}$). The equivalent width is then $EW_{filter} = -RW_{filter}[(F_{obs} - F_{phot})/F_{phot}]$. An additional modification to the White & Ghez procedure is made: because an R band measurement, F_R contains significant flux from $H\alpha$ emission, the $F_{H\alpha} - F_{phot}$ value is subtracted from F_R and a new estimate of F_{phot} is obtained. This loop is repeated a few times until convergence. The $H\alpha$ EWs and photosphere-subtracted fluxes are listed in Table 2. The 1997 EWs computed in the first iteration are consistent with those of White & Ghez (2001). Note that the EWs are negative-valued for emission. A couple of similar derivations for [S II] produced EWs around zero to within the errors, indicating little [S II] stellar emission, as one would expect. XZ Tau A’s $H\alpha$ emission varies as much as does XZ Tau B’s and with similar EWs. There is no correlation between the XZ Tau A $H\alpha$ EWs and R magnitudes. XZ Tau B shows a rough correlation, with the EWs generally lower as R becomes brighter.

The relative positions of the binary components at each epoch are given in Table 3. They have been converted to a geometrically undistorted coordinate system. Previous experiments have shown that the positional accuracy is typically ± 0.05 pixels for the PSF-fitting method. The position angles from the 2004 ACS images vary among the filters more than expected. For consistency, in addition to images taken in our program, we also fitted the F656N, F675W, and F814W images of XZ Tau that are described by White & Ghez (2001).

PSF-subtracted images of emission features nearest the binary are shown in Figures 4 and 5. There are significant residuals within $1''.0 - 1''.5$ of the stars and in the diffraction spikes, which are masked to avoid confusion. The processed images were geometrically corrected and then aligned to the midpoint of the binary and rotated to a common orientation based on the image header parameters.

4. Description of the *HST* XZ Tau/HL Tau Field

We describe here the large-scale features seen in the XZ Tau region, leaving detailed descriptions of the more transient outflow structures to section 4.2. Figures 1 and 2 show the 2004 ACS images of the field and the surrounding nebulae and young stellar objects. The two stellar components of XZ Tau have been subtracted. The major XZ Tau outflow extends outward along $PA=15^\circ$ and appears as overlapping bubbles within $6''$ of the binary.

The field is filled with reflection nebulosity. XZ Tau is situated within a relatively dark, roughly $49''$ by $28''$ elliptical region with the major axis along $PA 135^\circ$. The southwestern edge of this ellipse, $20''$ from XZ Tau, is bright in $H\alpha$ and corresponds to the emission source $H\alpha$ -A in Figure 3 of Mundt et al. (1990). This brightened “rim” is also seen in the WFPC2 WF2 R image. There is

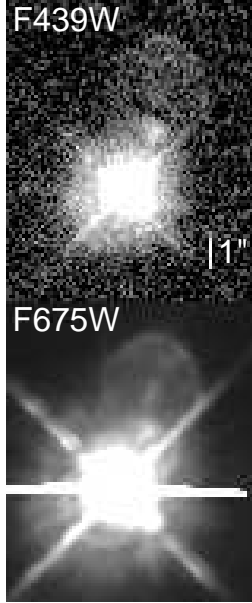


Fig. 3.— *WFPC2* F439W (*B*) and F675W (*R*) band images of the XZ Tau outflow from 1 Dec 1998. The images have not been PSF subtracted. Up is PA=33°

Table 2. XZ Tauri A & B Magnitudes and H α Line Strengths

Year	<i>R</i> mag		<i>I_c</i> mag		EW(H α) ^a Å		Flux(H α) ^b erg cm ⁻² s ⁻¹	
	A	B	A	B	A	B	A	B
1995	13.26	15.03	11.96	13.75
1997	13.60	15.52	11.98	14.10	-66	-161	5.4×10^{-13}	2.0×10^{-13}
1998	13.30	15.89
1999	13.56	15.06	11.96	13.44	-79	-153	6.6×10^{-13}	3.0×10^{-13}
2000	13.44	14.46	11.96	12.82	-194	-84	1.6×10^{-12}	3.0×10^{-13}
2001	13.34	12.84	-52	-92	5.5×10^{-13}	1.4×10^{-12}
2002	13.00	15.23	-173	-193	2.2×10^{-12}	3.1×10^{-13}
2004	13.36	16.07	-81	-197	9.2×10^{-13}	1.5×10^{-13}

^aEquivalent width; estimated errors are $\pm 8\%$.

^bPhotosphere-subtracted emission line flux; estimated errors are $\pm 8\%$.

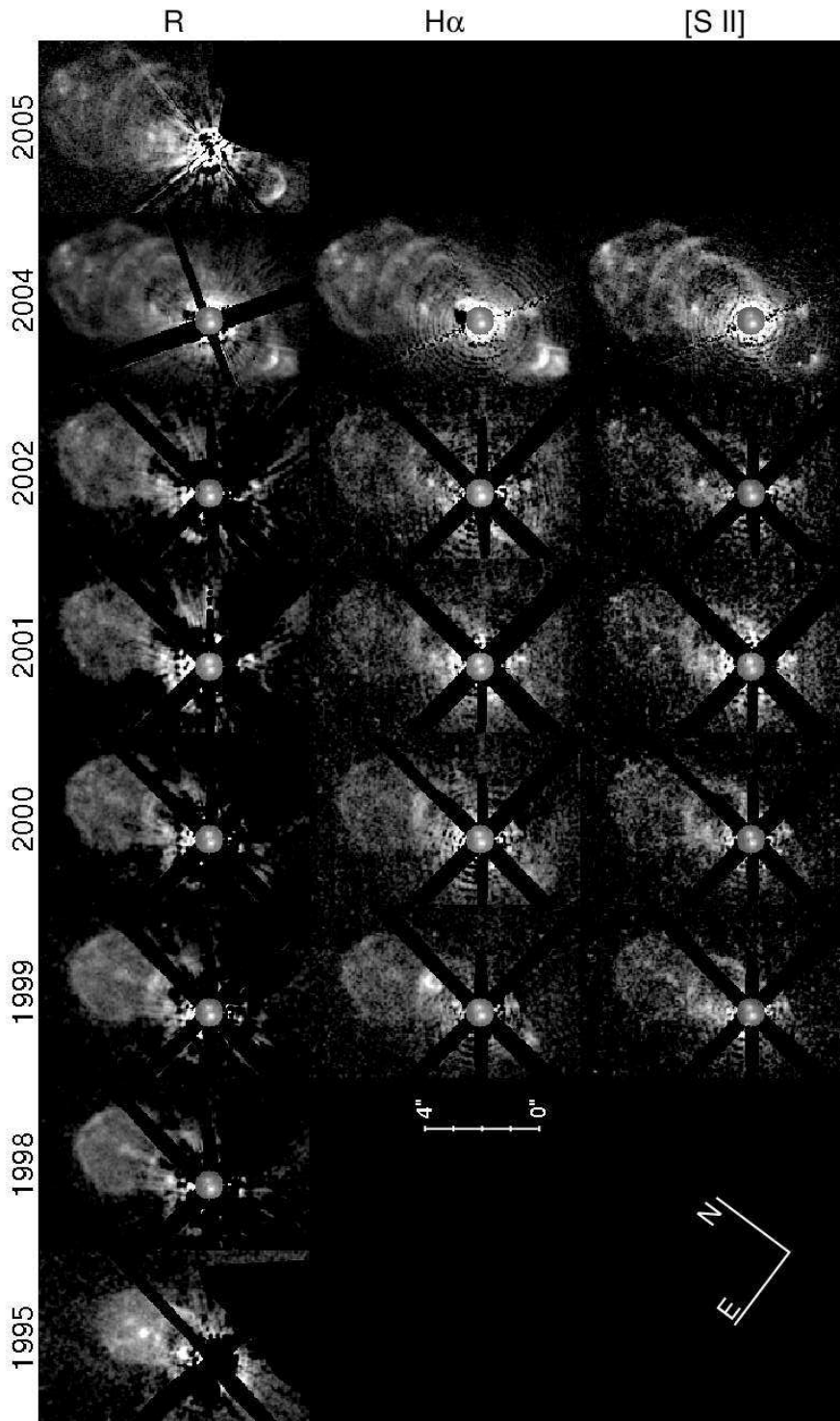


Fig. 4.— Subarrays of the XZ Tau images taken with WFPC2 and ACS displayed with a square-root intensity stretch. Short exposures of the binary have been superposed at a different intensity scale.

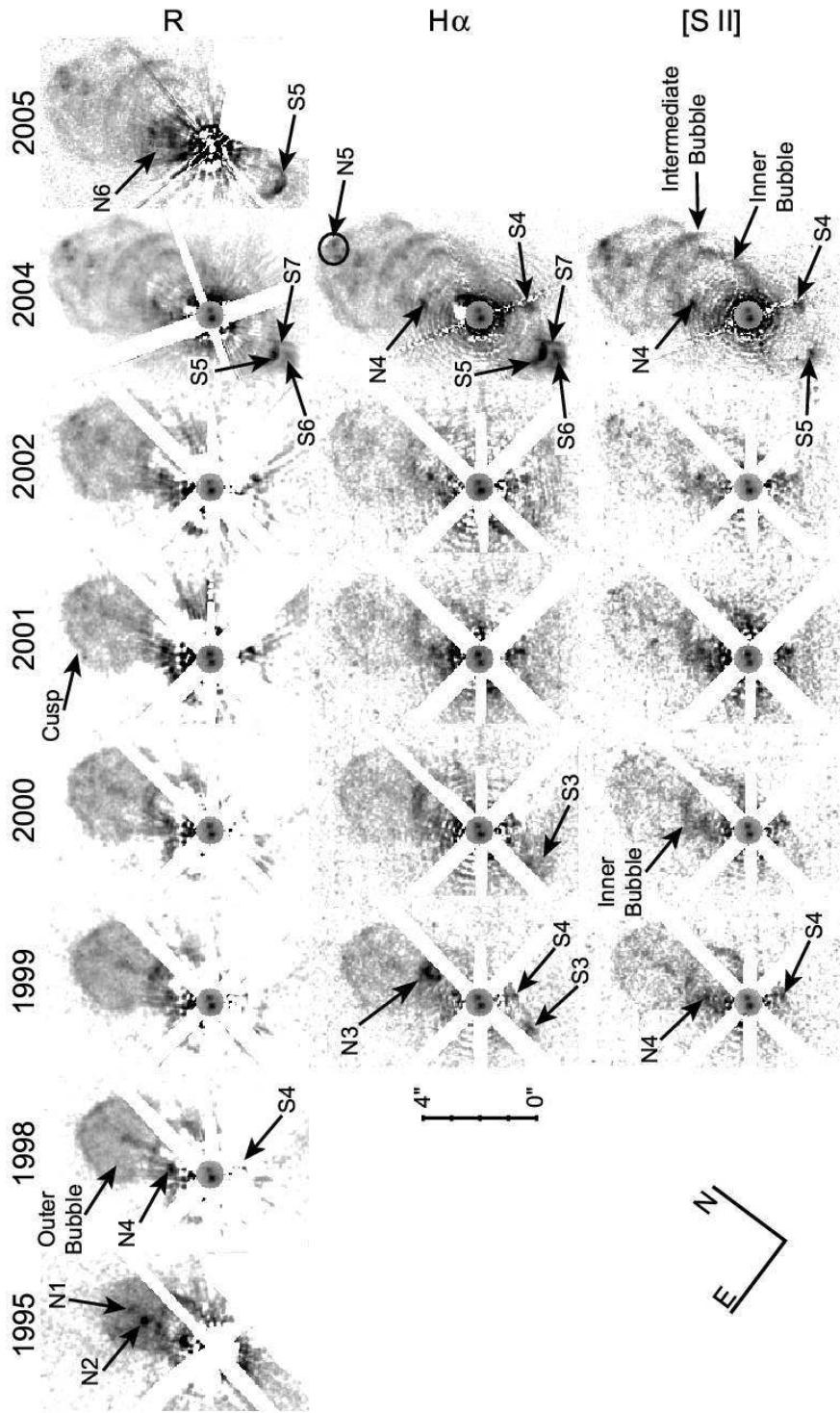


Fig. 5.— Intensity-inverted version of Figure 4 with features identified.

some H α emission extending perpendicularly from this edge back towards XZ Tau along the flow axis, with one small knot along it 19'' from the binary.

HL Tauri is the bright source 24'' W of XZ Tau and projected on the edge of the dark elliptical region. It is surrounded by reflection nebulosity. Our deep images show hints of broader bipolar cavities. The HL Tau jet (HH 150) is seen in both [S II] and H α emission along PA 51 $^\circ$, and is detected to distances of 40''. Oscillations in its path suggest that the jet may be slowly precessing with an angle of 3 $^\circ$ – 4 $^\circ$ from the axis of rotation or is being deflected by cloud material located approximately 20'' from HL Tau (interstellar material appears to be obliquely illuminated at that location). At that location the jet bends \sim 20 $^\circ$ to the N and into a complex of emission features known as HH 151¹. Our images show three H α -bright bowshocks spaced along HH 151, which exhibit greater transverse widths at greater distances from HL Tau. The [S II] emission here is more confined to the flow axis. Comparison of the 2004 and 1998 images shows outward proper motions for the bulk of this emission, except at its eastern edge which appears relatively stationary. On the SW side of HL Tau, a [S II]-bright knot is present \sim 6'' from the star along the flow axis.

The HH 153 complex extending \sim 11'' SE of HL Tau is seen primarily in [S II] emission. Our data confirms its apparent motion away from HL Tau, with slower proper motions for the most distant knots as seen by Movsessian et al. (2007). This region is referred to as H α -B and H α -C in Mundt et al. (1990). Movsessian et al. suggest that these may be part of a jet from LkH α 358 that is deflected by winds from XZ Tau. We do not see any evidence for an emission-line jet between these features and that object, which is located \sim 1 arcminute ESE of XZ Tau.

Figure 6 (provided in the Journal article) is an animated sequence of the 1998 WFPC2 WF2 and 2004 ACS *R*-band images that shows the motions of the outflows near XZ Tau and HL Tau.

The last major feature in the field is the HH 30 outflow and edge-on disk, seen 90'' S of XZ Tau. HST's multi-epoch view of the structure and proper motions of this flow will be presented in a future paper.

4.1. Properties of the Binary

The brightness of the southern component (XZ Tau A) varied in *R* between 13.0 – 13.6. During the four epochs for which there were both *R* and *I* measurements, it varied between *R*=13.26 – 13.60 but was constant in *I* (12.0). The presence of strong emission lines in *R* and the lack of them in *I* suggests that its overall variability is largely due to changes in the emission lines. However, there is no strict correlation between the derived photosphere-free H α fluxes (Table 2)

¹Early VLA maps suggested that a heavily embedded young star “HL Tau VLA 1” was present between HL and XZ Tau (Brown et al. 1985), and that HH 151 might be part of its outflow (Mundt et al. 1990). VLA 1 appears to be spurious, as its existence has not been confirmed by subsequent observations at any wavelength (Moriarty-Schieven et al. 2006). We therefore assume that HH 151 traces the outer parts of the main flow from HL Tau.

Table 3. XZ Tau Binary Mean Astrometry¹

Year	P.A. Degrees	Separation Arcseconds
1995	327.2	0.306
1997	326.0	0.300
1998	325.5	0.298
1999	324.4	0.301
2000	322.6	0.299
2001	321.6	0.297
2002	321.6	0.291
2004	322.3	0.294

¹The estimated errors are $\pm 0.5^\circ$ and $\pm 0''.003$.

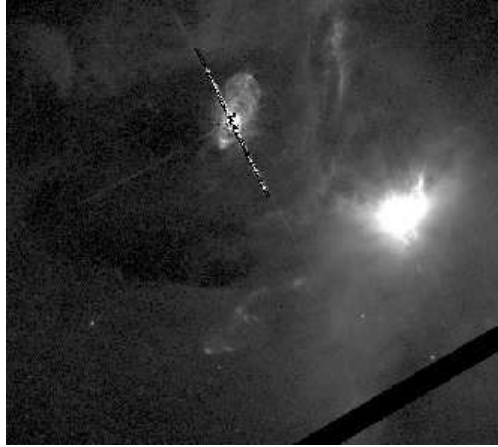


Fig. 6.— Animated sequence (available in the on-line version of the *Astronomical Journal*) of the 1998 WFPC2 WF2 and 2004 ACS *R*-band images of the XZ Tau/ HL Tau field. These illustrate the motions of the XZ Tau bubble (upper center), HL Tau jet (middle-to-upper right), and the HH 153 features (lower center). The field is $60''$ by $54''$. The stellar components have been subtracted in the ACS image. Up is $PA=33^\circ$.

and the R magnitudes, except that the maximum brightnesses for both occurs at the same epoch (2002). Excluding the data from 2000 would result in a rough correlation, so it might be possible that a jet knot was emitted during that epoch, contributing to an anomalously high $H\alpha$ flux.

XZ Tau B, in contrast, varies strongly in both continuum bands ($R=12.8 - 16.0$ and $I= 12.8 - 14.1$). Its $R - I$ color ranges from 1.3–1.6 but does not appear to be correlated with the stellar brightness. Its behavior indicates that the star’s variability is partly caused by changes in its underlying photosphere. In 2001, XZ Tau B increased in R brightness from the prior year by 1.62 mag and briefly became brighter than XZ Tau A (it was also brighter than A during the STIS observations of Hartigan & Kenyon (2003) that were taken in December 2000, two months prior to our 2001 visit). It was 2.39 mag fainter by early 2002. Its $H\alpha$ flux varies roughly in proportion to its R brightness, suggesting a variable accretion luminosity.

Over a nine year period, significant orbital motion has been observed in the binary. The position angle measured from A to B decreased by $5.0^\circ \pm 1.4^\circ$, while the separation decreased by $0''.013 \pm 0''.002$. These changes can be compared to theoretical timescales for orbital motion of the binary. White & Ghez (2001) compared the available stellar spectral information to evolutionary tracks, and derived a combined binary mass of $0.95M_\odot$. A lower limit to the binary’s orbital semi-major axis can be obtained by assuming that the system is currently near apoastron, and that the projected separation was equal to the physical separation. In this case a would be just 21 AU (half the projected separation), the minimum orbital period would be 99 years, and the orbit would have to be highly eccentric ($e \sim 0.9$) to account for the small position angle motion that is observed. The binary separation is currently decreasing, so the last apparent periastron passage must have taken place at least one-half period before the present date, or approximately 1955. Allowing for the unknown projection angles, the orbital period is likely to be longer and the eccentricity smaller than these values. Since the likely dates of the eruption which produced the N outflow bubbles are much more recent (Krist et al. 1999), it is unlikely that their ejection was triggered by the most recent periastron passage (Bonnell & Bastien 1992).

4.2. Structure and Evolution of the XZ Tau Outflow

Because the outflow structures show significant evolution from one year to the next, we provide a narrated description of the changes here. Noteworthy emission knots in the flow are assigned the prefixes N and S indicating whether they are found north or south of the binary. The emission features discussed below are labeled on the individual epoch images show in Figure 5.

1995: These are the original discovery images first discussed by Krist et al. (1997). The outer bubble extended $4''.3$ north of the binary along $PA=15^\circ$. Near its center was a bright knot, N2, located $2''.6$ from the binary. A fainter knot, N1, was located at $3''.1$, and knot N4, seen more clearly at later epochs, was at $1''.1$. A limb-brightened inner bubble or shell, $2''$ in diameter, was centered $\sim 1''.5$ from the stars. No outflow features were seen on the southern side of the system.

1998: The outer bubble expanded to $5''.0$ in length and became limb-brightened. Several condensations were present along this limb. Knot N2 faded considerably and had a $0''.5$ -long trail. Knot N1 could not be reliably identified. It appears to have fragmented, judging from later epochs. Knot N4 moved further from the stars, and knot S4, which would become more prominent at later epochs, appeared at an equal distance from the stars on the southern side. The motions of N4 and S4 at later epochs indicate that they are part of a collimated jet emitted by XZ Tau B aligned along $PA=36^\circ$. Additional discussion of this epoch can be found in Krist et al. (1999).

1999: The nebula appeared much as it did in R in 1998, with an expansion of the outer bubble to $5''.2$ in length. This was the first epoch with $H\alpha$ and [S II] narrowband images, and significant differences between the lines were evident. The inner bubble's limb was brighter than the outer's in R and [S II] and was weak in $H\alpha$. A bright, nearly circular knot, N3, was seen at the forward edge of the inner bubble. It was obvious in $H\alpha$ and in the late 1998 WFPC2 F439W and F675W frames (Figure 3) but was not clearly visible in [S II] except along its forward edge, and so it was likely to be a high energy shock. An equidistant knot S3, on the southern side of the binary, is again seen in $H\alpha$ but not [S II]. It had a sharp western edge while the eastern extension appeared to curve away from the stars. Knots N4 and S4 were symmetrically located $\sim 1''.4$ on opposite sides of the binary and were seen in both emission lines. Knot N2 faded, and the emission line images revealed that its forward edge emitted in $H\alpha$ but its "tail" emitted in [S II].

2000: The N outer bubble extended to $5''.4$ and its forward edge was heavily fragmented. An indentation or "cusp" appeared along its NE edge, while the knots along its forward edge (e.g. N5) became brighter. The intensity of the outer bubble's limb decreased. Knot N3 faded, leaving only a faint remnant along its western edge visible in $H\alpha$. The inner bubble was well defined in [S II]. Knot S3 became fan-shaped, opening away from the stars, and was seen in $H\alpha$ but not [S II].

2001: The forward edge of the outer bubble was $5''.6$ from the stars, and in $H\alpha$ was displaced $\sim 0''.1$ further out than in [S II]. The forward half of the bubble was brighter than the trailing half. The cusp was more pronounced than before. Knots N4 and S4 brightened, while S3 disappeared. The northern star, XZ Tau B, increased in brightness by 1.6 magnitudes in R relative to 2000 and was 0.5 mag brighter than XZ Tau A.

2002: The N outer bubble extended to $5''.7$ from the stars. The cusp was becoming more distinctive and was also seen along the W side of the outer bubble as well. The E forward edge of the outer bubble was more strongly limb brightened than the W side. Several knots just inside the edge of the outer bubble, some of which may have been remnants of knot N1, became visible.

2004: The N outer bubble extended to $6''.0$. The knots at the bubble apex brightened in all three filters. The inner bubble appeared as a $3''$ diameter shell with the S edge overlapping the stars. Its forward edge was flattened and was fainter its W and E edges. Between the inner and outer bubble a new, broad arc was visible at $3''.7$ from the stars. This appeared to be the bright, forward edge of a faint bubble (the "intermediate bubble") whose E and W sides are faintly seen in Figure 7. This bubble is wider ($4''.7$ diameter) than it is long. In F658N a faint $2''.2$ long arc is seen $12''.9$ N

of the binary near, and oriented perpendicular to, the outflow axis. To the south of the binary, a bright, $1''$ -wide bowshock (S5) appeared $2''.8$ away, opposite of the northern outflow. The arc was prominent in R and $H\alpha+[N\ II]$ but was faint in $[S\ II]$, except for a central knot. S5 was bounded on its western edge by a straight segment of emission (S7), visible in $H\alpha+[N\ II]$ and faintly in $[S\ II]$. This segment radially extended $\sim 1''$ further from S5 towards another new knot, S6, located $3''.5$ from the stars. S6 was visible in R and $H\alpha+[N\ II]$ but not at all in $[S\ II]$. The direction and position of S5 and S6 suggest a possible relationship with the earlier knot S3. Along the same direction as S5 and S6 a faint, $5''$ diameter bubble was centered $4''.8$ from the stars (Figure 7). This bubble was too faint to be seen in the previous WFPC2 images. It was best seen in $H\alpha+[N\ II]$ and faintly in $[S\ II]$. In R its outer region blended into the background reflection nebulosity. The forward, S edge of this bubble appeared slightly brighter than the interior, suggestive of limb brightening. There is a dark, circular region within the bubble. Figure 2 shows that $15''.3$ south of the binary, a faint streak of $H\alpha$ emission extended $4''.5$ along the XZ Tau A jet axis at $PA=197^\circ$. A knot, S8, was located along this streak $19''$ from the stars. The streak terminated perpendicularly to the broad feature $H\alpha$ -A, as discussed above. Knots N4 and S4 in the XZ Tau B jet were prominent in both $H\alpha$ and $[S\ II]$ (S4 was partially occulted by a PSF diffraction spike). A small curved structure extending out to $0''.8$ north from the binary appeared, and was perhaps another new emission knot.

2005: The outer bubble extended to $6''.1$. The knots along its forward edge faded slightly. The northern region of the outflow within $2''.5$ of the stars (N6) brightened. S5 appeared to have transformed into a thin arc that curved around behind the forward edge. S6 was not seen.

4.3. Identifying XZ Tau A as the Primary Outflow Source

As previously noted, XZ Tau B is the most active component of the binary as evidenced by its photometric variations and rich accretion features. Without measuring the motions of all of the knots over the various epochs, it would seem straightforward to assign the source of the bubbles and most prominent jet features to B. However, our images have sufficient resolution and time coverage to show that is not the case.

If we track only the outermost knots (N5) in the jet that bisects the outer N bubble, then there is enough dispersion in that knot group to perhaps allow XZ Tau B to be its source. However, a line drawn through those knots and B would entirely miss all of the southern knots, including S4, and the southern bubble. It would lie outside the perimeter of the S5 bow shock as seen in 2005. In contrast, a line drawn through all of the knots except N4 and S4 aligns well with XZ Tau A. N4 and S4 are aligned with XZ Tau B along $PA=36^\circ$. Their equal velocities and distances from B strongly suggest that they are associated. They are clearly not aligned with A. Their motions are also lie along the same position angle. While it may be possible to presume that N4 might be part of a shock along a bubble rather than a jet knot, it does not seem likely that S4, with no other surrounding nebulosity, can be so disassociated.

We associate the XZ Tau A jet with the outer N and S bubbles. Their axes of symmetry are aligned with the A jet. The N “inner” bubble does appear to have different symmetry axis, though because it is clearly interacting with the outer bubbles, this may more likely be due to nonuniform densities in the interface with those bubble rather than with interaction with a flow from XZ Tau B.

4.4. XZ Tau Outflow Proper Motions

The XZ Tau outflow has a number of components: the extended northern and southern bubbles, the collimated XZ Tau A jet (including knots N2, N3, S3, N5, S5, S6, and S8) along PA=15° , and the collimated XZ Tau B jet (knots N4 and S4) along PA=36° . The broad H α -A feature is also assumed to be associated with the XZ Tau A outflow. At each epoch the distances of the flow features from the binary midpoints (Table 4) were measured by visually estimating their centers. For bow-shaped structures like S5 the positions of the forward edges were measured. Because some of the knots and shocks were irregular (*e.g.* S3) or changed shape over time (*e.g.* N2), there may be position errors of 0''.05 – 0''.12. Also, some knots may not have been unambiguously separated from subtraction residual artifacts. The motions between epochs were converted to mean projected velocities (Table 5). The mean velocity of H α -A was derived by aligning the 1998 WF2 and 2004 ACS *R* images to the binary midpoint and then iteratively shifting and subtracting the 1998 image until the feature disappeared.

To accurately measure the velocity of the forward edge of the outer northern bubble, each of the PC1 *R* and ACS F625W and F606W images was registered to binary midpoint and then magnified until the forward edge was aligned with itself in the 2002 image, as judged by subtraction (Figure 8). The magnifications were then converted to velocities (Table 6). The unmagnified and magnified sequence of images are shown in animated form in Figures 9 and 10 in the Journal article.

The XZ Tau A jet is the fastest of the outflows (judging by knots N2 and S5), with tangential velocities of up to $\sim 200 \text{ km s}^{-1}$. This jet and the outer bubble appear to terminate at the same location in the North at knot N5, which has approximately the same velocity as the outer bubble’s leading edge at the latest epoch. The forward edge of the outer bubble had a mean outward velocity of $\sim 130 \text{ km sec}^{-1}$ in the early epochs and decelerated to $\sim 93 \text{ km sec}^{-1}$ by 2001 – 2002. Afterwards, there was a small increase in velocity to $\sim 110 \text{ km sec}^{-1}$. This apparent increase could have been caused by unseen gas just beyond the limb that began to emit between 2002 – 2004. The H α -A feature had a mean velocity of 100 km s^{-1} between 1999–2004. The XZ Tau B jet had a velocity of $\sim 100 \text{ km s}^{-1}$, judging by knots N4 and S4.

Hirth et al. (1997) measured a maximum radial velocity of -70 km s^{-1} at 1''.4 N from the stars in late 1992. This likely corresponded to either the the center-brightened outer bubble or the forward edge of the inner bubble. Assuming a tangential outflow velocity of $\sim 140 \text{ km s}^{-1}$, this implies an inclination of $\sim 27^\circ$ from the plane of the sky with the N flow approaching.

The width of the bubble was determined by plotting lines parallel to the jet axis along the bubble edges. The derived mean transverse velocities ranged from $46 - 76 \text{ km s}^{-1}$. The lowest velocity occurred between 2002 – 2004 and the highest in the next interval, 2004 – 2005. This discrepancy could be caused by gas just outside the visible limb in 2004 beginning to emit in 2005, creating an apparent acceleration.

Given the lack of earlier data, we assume that the N outer bubble’s 1995 – 1998 mean transverse velocity of $\sim 65 \text{ km s}^{-1}$ represents its actual radial expansion velocity prior to that period. During this time, the forward edge of the N outer bubble had a measured outward velocity of 130 km s^{-1} . This implies that the center of the bubble, located $3''.2$ from the stars in 1995, had an apparent velocity along the jet axis of $130-65= 65 \text{ km s}^{-1}$. This is considerably less than the $> 150 \text{ km s}^{-1}$ velocity of the XZ Tau A jet (as measured by knot N2). An extrapolation of the transverse and forward velocities indicates that the bubble would have had an apparent zero width ~ 28 years earlier at a position $\sim 0''.5$ from the stars.

The animated image sequences in Figures 9 and 10 (provided in the Journal article) reveal the apparent motion of material just inside the limb of the outer bubble. These diffuse patches are difficult to identify in individual images. Their velocity is about half that of the forward edge, and in the magnified image sequence, where the forward edge is aligned, they appear to move backwards from it. These patches may be bubble material entrained on the ambient medium.

4.5. Emission Line Images

The emission line images indicate significant differences in the excitation energies within the nebulae. $\text{H}\alpha$ emission corresponds to shock velocities of $V_s \sim 80 - 100 \text{ km s}^{-1}$, while [S II] emission comes from lower excitation gas with $V_s \sim 40 \text{ km s}^{-1}$ (Reipurth & Bally 2001). $\text{H}\alpha$ emission clearly dominates in the rapidly appearing and disappearing shocks created by the fast XZ Tau A jet (e.g. N3, S5, S6). The remainder of the nebulae emit in more equal parts of $\text{H}\alpha$ and [S II], including the slower XZ Tau B jet knots.

The outer bubble’s limb along the cusp was coincident in both lines in 1999 and 2000 but was displaced outwards in $\text{H}\alpha$ by $0''.05 - 0''.15$ in 2001–2004 relative to [S II]. Both lines together account for only about half of the total outer bubble flux measured in the R band image, so it is likely that there is significant emission from [O I] (6300 \AA) and/or [N II] (6548 \AA) ([O I] indicates lower excitation gas than [N II], which is comparable to [S II]).

The lower resolution WFPC2 B band (F439W) image from December 1998 (Figure 3) shows emission along the forward edge of the outer bubble and in knot N3. The most prominent HH emission lines included in the F439W bandpass are [S II] 4069, 4076 \AA and the $\text{H}\gamma$ line (Solf et al. 1988). However, three months later, there was no sign of N3 in the PC1 [S II] 6717+6731 \AA image but it was bright in $\text{H}\alpha$. This suggests that the F439W emission may have primarily been $\text{H}\gamma$, corresponding to a $\sim 100 \text{ km s}^{-1}$ shock.

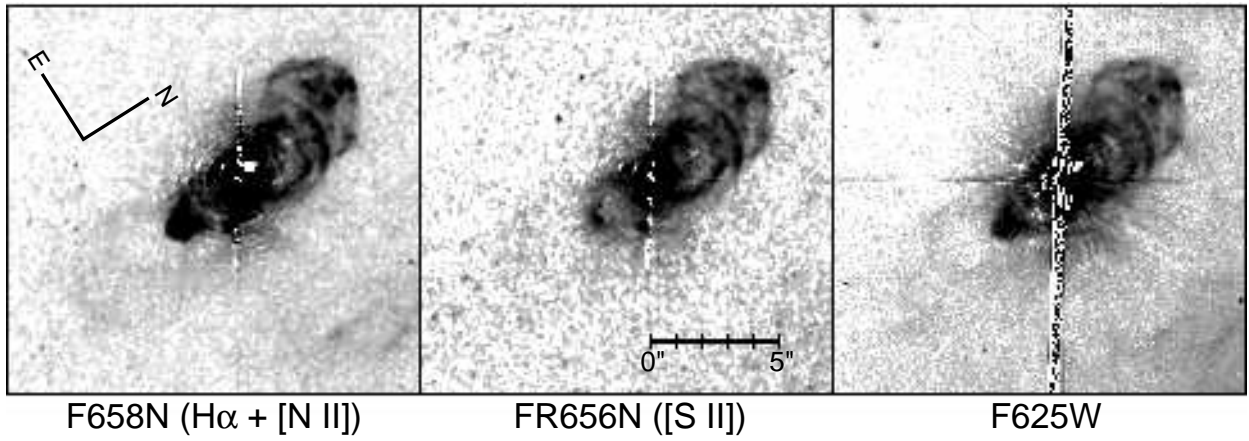


Fig. 7.— ACS F658N, FR656N, and F625W images from 2004 stretched in intensity to reveal the faint bubble along the southern XZ Tau outflow.

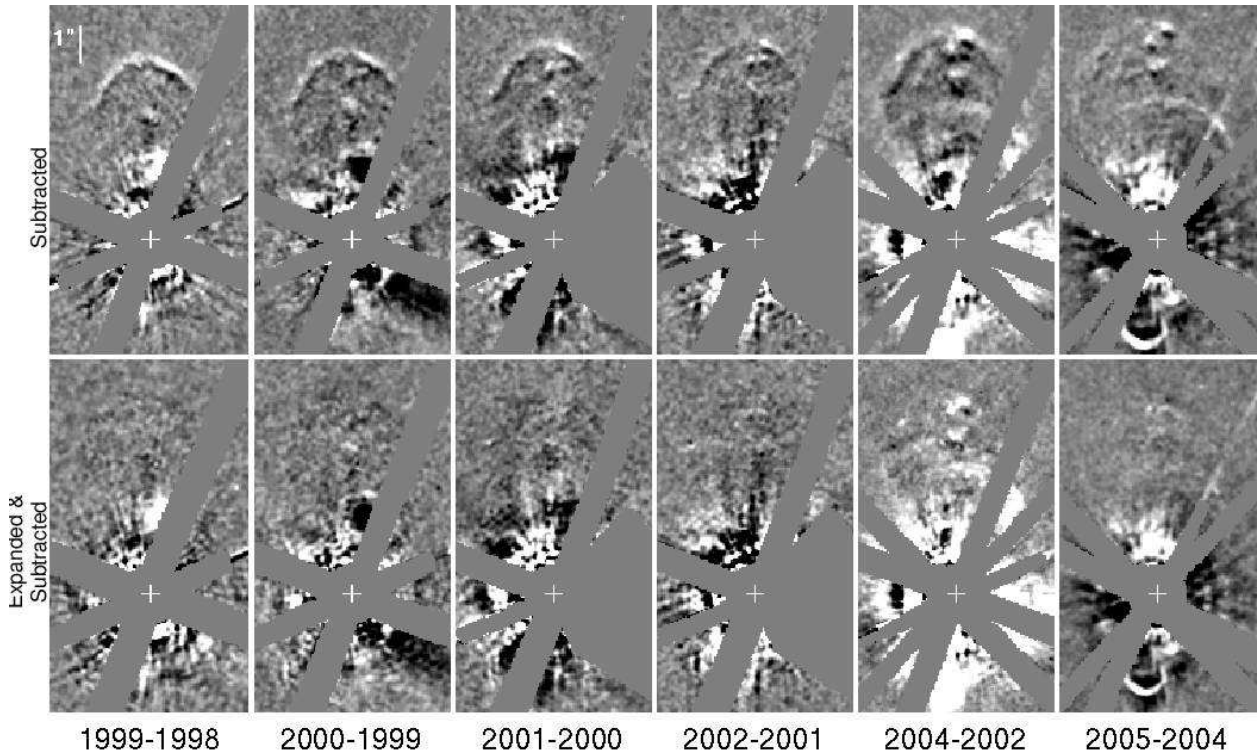


Fig. 8.— (Top) WFPC2 and ACS PSF-subtracted R -band images of XZ Tau showing the difference between each epoch and the one preceding it. (Bottom) The differences after the image from each epoch was magnified so that the forward edge of the bubble was aligned to itself in the 2002 image. Up is $PA=15^\circ$.

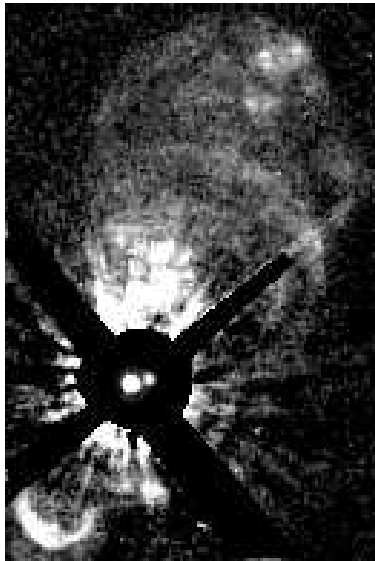


Fig. 9.— Animated sequence (available in the on-line version of the *Astronomical Journal*) of PSF-subtracted, long-exposure, *R*-band images of XZ Tau taken between 1995 – 2005. Unsaturated images of the stars from short exposures have been superposed.



Fig. 10.— Animated sequence (available in the on-line version of the *Astronomical Journal*) of PSF-subtracted, long-exposure, *R*-band images of XZ Tau taken between 1995 – 2005. Unsaturated images of the stars from short exposures have been superposed. The images have been magnified so that the forward edge of the outer bubble is aligned at each epoch. Note that the jet from XZ Tau A is moving faster than the forward edge of the bubble.

4.6. Nebulae Photometry

The fluxes of the compact knots and bow shocks in the narrowband images were measured using visually-defined irregular apertures after subtraction of the local background measured in adjacent regions. Because of the changing shape of the features, these fluxes are assumed to be rough measures with errors for the fainter knots approaching 50%. The instrumental count rates were converted to emission line fluxes (Table 7) using the equations in the WFPC2 and ACS Instrument Handbooks. The ACS F658N fluxes include contributions from both $H\alpha$ and $[N II]$.

The mean surface brightnesses of the outer bubble are given in Table 6, measured in regions excluding the inner bubble and XZ Tau A jet knots. The overall bubble brightness decreased substantially between 1995 – 1998, but has fallen slowly thereafter. The mean integrated $H\alpha/[S II]$ and $H\alpha/R$ flux ratios (corrected for filter efficiencies) were derived by iteratively multiplying the denominator images by a constant and subtracting them from the $H\alpha$ frames until the outer bubble was visually minimized (ignoring the knots at the bubble’s apex). The estimated errors are 15%. From 1999 – 2002 the $H\alpha/[S II]$ ratio varied between 1.2 – 1.7. $H\alpha$ contributed 30% – 40% of the R band flux while $[S II]$ added 20% – 30%. The remaining R band flux was likely dominated by $[N II]$ and lesser amounts of $[O I]$ and $[O II]$. In 2004, the $(H\alpha+[N II])/[S II]$ ratio was 1.8, with $H\alpha+[N II]$ contributing $\sim 53\%$ of the R band flux, with 30% from $[S II]$. Assuming the $H\alpha/R$ from the previous epoch, this would suggest that $[N II]$ emission is $\sim 23\%$ of the R flux.

It can be demonstrated that the interior of the outer bubble in 1998 and later was actually filled with emission, as it was in 1995, rather than being a luminous, hollow shell. To quantify the contribution of volumetric emission to the observed surface brightness, model spherical shells of $0''.15$ thickness were subtracted from the images, with their diameters, positions, and amplitudes adjusted until the limb was visually minimized (as the forward edge became less circular at later epochs, the shell was fit only along the NE edge). After subtraction of the model shells, there was still considerable residual flux whose origin we ascribed to the bubble interior (Figure 11).

5. Discussion

The nine epochs of HST imaging reveal a complex combination of outflows from both stars and their interaction with the surrounding medium. Each star has a collimated, bipolar jet. Large bubbles are aligned along the XZ Tau A jet axis. Knots in the XZ Tau A jet move through these bubbles and are seen catching up with the apex of the outer bubble, a few arcseconds N of the binary. The S side of the flow shows a faint counterpart to the outermost N bubble, and two interior, compact, bow-shaped knots that suddenly appeared in 2004. Evidence for a more extended flow to the N is seen in ground-based images, and to the S extending to distances of $20''$ where the $H\alpha$ -A structure is found oriented perpendicular to the jet. In comparison, the visible portion of the XZ Tau B jet consists of only knots N4 and S4 that show proper motions about half those of the fastest XZ Tau A knots. It is clear that XZ Tau A is the dominant outflow source in the system, which is

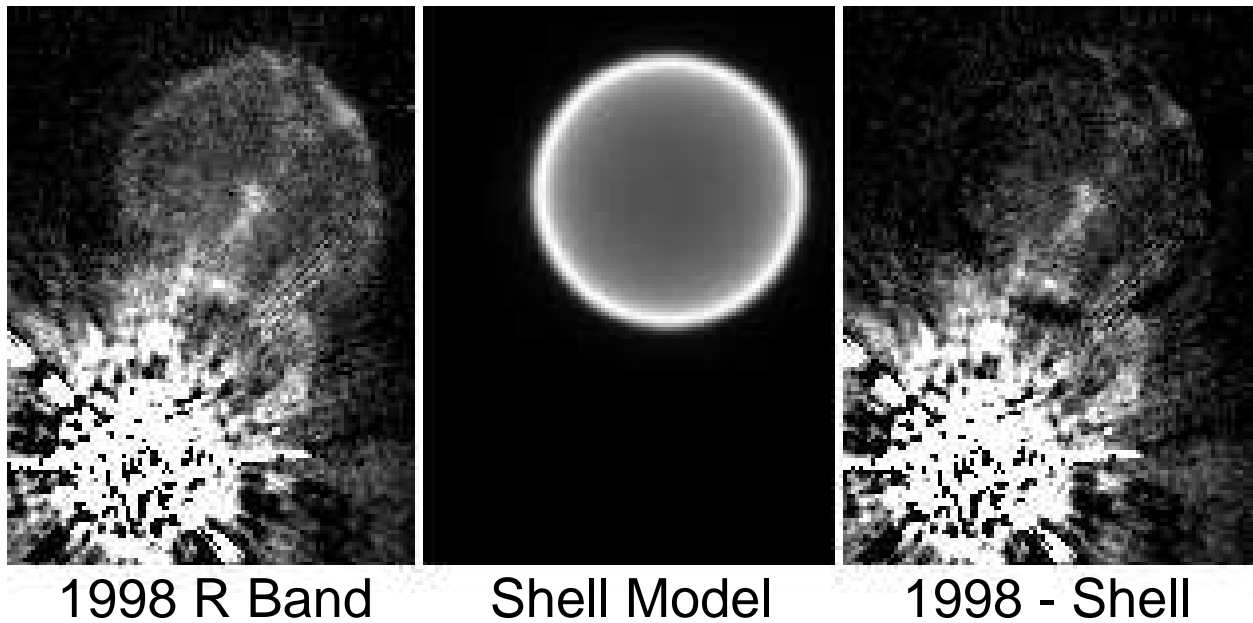


Fig. 11.— Demonstration that the interior of the limb-brightened XZ Tau outer bubble contained emitting material. (Left) *R* band image of the bubble in 1998. (Middle) Model of a spherical shell matched to the limb-brightened edge of the bubble. (Right) Subtraction of the shell model from the data revealing residual interior flux.

Table 4. XZ Tau Knot Distances (Arcseconds) from Binary Midpoint^a

Year	N1	N2	N3	S3	N4	S4	N5	S5	S6
1995	3.10	2.58	1.14
1998	...	3.35	1.53
1999	...	3.60	2.15	1.97	1.59	1.26
2000	...	3.84	...	2.09	1.65	1.32	5.15
2001	...	4.14	1.78	1.51	5.33
2002	...	4.40	1.88	1.66	5.45
2004	...	4.79	2.10	1.85	5.76	2.79	3.51
2005	...	4.97	2.20	1.88	5.90	3.04	...

^aEstimated errors are $\pm 0'.05$.

Table 5. XZ Tau Mean Knot Velocities^a (km s⁻¹)

Year	N2	S3	N4	S4	N5	S5
1998	159	...	81
1999	193	...	45
2000	158	79	40	39
2001	197	...	85	125	118	...
2002	172	...	66	99	79	...
2004	134	...	75	65	107	...
2005	125	...	69	21	97	174

^aEstimated errors are ± 30 km s⁻¹.

Table 6. XZ Tau Outer Bubble Parameters

Year	Mean Surface Brightness ^a erg cm ⁻² sec ⁻¹ arcsec ⁻²	Mean H α /[S II] Flux	Mean H α / <i>R</i> Flux	Length ^b arcsec	Maximum Width arcsec	Longitudinal Velocity km s ⁻¹	Transverse Velocity km s ⁻¹
1995	1.3×10^{-14}	4.33 ± 0.03	2.72 ± 0.06
1998	6.5×10^{-15}	4.95 ± 0.02	3.34 ± 0.06	130 ± 8	65 ± 10
1999	6.2×10^{-15}	1.7	0.40	5.14 ± 0.02	3.53 ± 0.06	138 ± 20	69 ± 33
2000	5.3×10^{-15}	1.4	0.40	5.33 ± 0.02	3.68 ± 0.06	125 ± 18	50 ± 30
2001	5.5×10^{-15}	1.2	0.30	5.51 ± 0.02	3.86 ± 0.06	118 ± 18	59 ± 30
2002	5.1×10^{-15}	1.6	0.30	5.65 ± 0.02	4.01 ± 0.06	93 ± 19	50 ± 30
2004	4.1×10^{-15}	1.8 ^c	0.53 ^c	5.98 ± 0.02	4.28 ± 0.06	113 ± 10	46 ± 16
2005	4.1×10^{-15}	6.14 ± 0.02	4.50 ± 0.06	111 ± 19	76 ± 32

^aMeasured in *R* assuming all emission at $\lambda = 656 \text{ \AA}$.

^bMeasured from binary midpoint.

^c2004 ACS H α measurement includes [N II] emission.

Table 7. XZ Tau Knot Fluxes^a (erg cm⁻² sec⁻¹)

Year	N2	N3	S3	N4	S4	N5	S5	S6	S7
H α									
1999	4.8×10^{-17}	3.2×10^{-15}	8.8×10^{-16}	7.2×10^{-17}	1.9×10^{-16}
2000	2.8×10^{-16}	5.4×10^{-17}	2.1×10^{-16}	$< 3.0 \times 10^{-17}$
2001	2.5×10^{-16}	4.8×10^{-16}	$< 2.4 \times 10^{-17}$
2002	4.4×10^{-16}	7.3×10^{-16}	$< 6.6 \times 10^{-17}$
2004	4.1×10^{-16}	7.1×10^{-16}	3.3×10^{-16}	3.3×10^{-15}	3.0×10^{-15}	8.9×10^{-16}
[S II]									
1999	1.8×10^{-16}	6.5×10^{-17}	...	3.8×10^{-17}	5.9×10^{-17}
2000	3.8×10^{-17}	1.2×10^{-16}	$< 2.7 \times 10^{-17}$
2001	1.8×10^{-16}	3.3×10^{-16}	1.0×10^{-16}
2002	1.3×10^{-16}	8.6×10^{-17}	3.8×10^{-17}
2004	1.3×10^{-16}	1.9×10^{-16}	1.3×10^{-16}	2.7×10^{-16}

^aEstimated errors are $\pm 20\%$ for brightest knots, $\pm 50\%$ for the faintest. No extinction corrections have been applied.

surprising given that XZ Tau B is much more photometrically variable and has a more prominent emission line spectrum.

5.1. Origin of the Bubbles

The XZ Tau bubbles are unlike the large bowshocks seen in other Herbig-Haro flows and numerically modeled by various workers. A prototypical bowshock represents the interaction region where a narrow, fast-moving jet impacts material along the flow axis. The impacted gas can be either ambient interstellar material, or slower-moving ejecta output previously by the source. The brightest emission and highest excitation is found at the bowshock apex, where normal incidence of the flow along the jet axis creates the largest shock velocity difference. Lower shock velocities at oblique angles along the sides of the bowshock produce fainter emission and weaker excitation along the trailing bowshock wings. Examples include the HH 1 and HH 34 systems (Hester et al. 1998; Reipurth et al. 2002), and the $H\alpha$ emission structures at northern limit of the HL Tau jet in Figure 2. In comparison, the XZ Tau bubbles lack the characteristic peak brightness and excitation at their apex; the outer bubble becomes limb-brightened, fades, decelerates, and deforms along its leading edge over a period of less than 10 years; and the flow has a large opening angle $\sim 30^\circ$ near the source. Taken together, these features suggest that the outer bubble is largely “coasting” on the initial momentum with which it formed, with little ongoing energy deposition from the flow of a continuous jet.

We now sketch out a scenario for the origin and evolution of the N outer bubble in the XZ Tau outflow. It cannot be the result of a wide-angle, ballistic ejection from the star given that it appears limb-brightened in 1998-1999 along more than just its forward edge. Instead, the spherical symmetry of the bubble in the early epochs suggests radial expansion of an initially hot, compact gas parcel carried along in the general outward flow from XZ Tau A. The observed transverse proper motions of the bubble (70 km s^{-1} ; see Table 6) suggest a characteristic initial energy for the bubble. We postulate that the XZ Tau A stellar jet underwent a large velocity pulse circa 1980. This ejection quickly overtook older, slower-moving ejecta very near the star, producing a $\sim 70 \text{ km s}^{-1}$ shock in a hot ($T \sim 80,000 \text{ K}$), compact “fireball”. The initial pressure of this gas parcel created an expanding hot bubble within the flow, but rapid cooling terminated this early inflationary stage and left a ballistically expanding cloud carried along at the mean longitudinal velocity of the flow. Surrounding material swept up in the radial expansion of the bubble led to the formation of a shell, which took on the appearance of a limb-brightened emission bubble when the shell became dense enough for enhanced cooling and/or enough time had elapsed for the post-shock $H\alpha/[S \text{ II}]$ cooling zone to form. The forward edge of the bubble has preferentially slowed and deformed as it encounters higher downstream densities found in the wakes of previous ejections along the flow axis. Subsequent jet velocity pulses have led to the formation of additional shells trailing the bright outer bubble.

The southern bubble, seen only in 2004, is sufficiently similar to the N one in appearance to

suggest a common origin in a symmetric velocity pulse in bipolar jets. The S bubble is slightly larger and centered further from the binary than the N one, and is much fainter. It lacks the complex internal knots seen within the N bubble. Because the S bubble is detected at only one epoch, it is unknown if it transitioned from an internally-brightened to limb-brightened nebula as the N bubble did. It is clear that the N bubble has encountered material dense enough to decelerate and deform its forward edge, creating the cusps. The faintness and relative simplicity of the S bubble suggest that it is expanding into a more rarified and uniform medium than the northern one.

Coffey et al. (2004) studied the 1995 – 2001 epochs from our dataset and suggested that XZ Tau B was an eruptive, EXor-type star based on its spectral lines and photometric variability and thus was the likely source of the bubbles. Without using PSF-subtracted images or tracing knot motions through later epochs, they did not recognize that both stars have jets and that the bubbles are aligned with the XZ Tau A jet. They modeled the formation of the outer bubble as the result of a 250 km s^{-1} stellar wind with an opening angle of 22° , with the collimated jet having no significant effect. This scenario, however, does not suitably explain the appearance of the bubble in 1995, the multiple bubbles and their curvatures, or the finite apparent length of the northern outflow. The interaction of slow and fast moving knots from XZ Tau A seem to better explain these characteristics.

5.2. The Jets

The extended emission bubbles of XZ Tauri enclose multiple compact emission knots which attest to the continued flow of bipolar jets after the bubble ejection events. The position and proper motions of knots N4 and S4 point to XZ Tau B as their source and a flow PA of 36° . Both steadily brightened by a factor of ~ 5 between 2000 and 2004. All of the other observed knots are associated with the jet from XZ Tau A along PA 15° , and show more transient brightness variation. On timescales of just a year or two, knots N1, N2, N3, and S3 completely faded from view. This requires relatively high gas densities within the knots so that rapid cooling and recombination can take place. Conversely, S5 and S6 appeared suddenly in 2004 as the brightest and fastest-moving knots in the entire outflow, but were entirely absent two years previously. The jet’s encounter with a sharp density discontinuity in the pre-shock medium at this epoch (likely a structure in the wake of prior ejections) would account for this. S5 appears the most bowshock-like of all the jet knots, showing both extended curved wings and a bright spot at its apex.

5.3. A Trial Model for the XZ Tau A Outflow

Numerical simulations of Herbig-Haro jets tend to focus on the structure of the classical jet/bowshock working surface at large propagation distances from the outflow source. For comparison to the XZ Tau bubbles, simulations of a very young pulsed jet are needed in the region very

close to the outflow source. We have begun to explore such models using a third-order WENO (weighted essentially non-oscillatory) method (Shu 1995) for supersonic astrophysical flow simulations (Ha et al. 2005). WENO schemes are high-order finite difference methods designed for nonlinear hyperbolic conservation laws with piecewise smooth solutions containing sharp discontinuities like shock waves and contacts. Locally smooth stencils are chosen via a nonlinear adaptive algorithm to avoid crossing discontinuities whenever possible in the interpolation procedure. The weighted ENO (WENO) schemes use a convex combination of all candidate stencils, rather than just one as in the original ENO method.

We simulated an approximation to the northern jet outflow and a pair of expanding bubbles, including the effects of radiative cooling using the cooling function from Figure 8 of Schmutzler & Tscharnuter (1993). Two-dimensional simulations were performed on a $750\Delta x \times 750\Delta y$ grid spanning 10^{11} km on each side. The jet has a width of 10^{10} km, and inflows at Mach 15 with respect to the sound speed in the light ambient gas and Mach 55 with respect to its own internal soundspeed. Other flow parameters of the simulation are summarized in Table 8, and atomic gas ($\gamma = 5/3$) is assumed. The leading edge of the resulting outer bubble propagates initially at 150 km s^{-1} , decaying to 90 km s^{-1} at 24 years, with an average velocity over this period of 120 km s^{-1} .

The jet was pulsed: a first pulse was turned on for 0.4 yr, and then the jet inflow was turned off for 8.6 yr while the first pulse propagated. Next a second pulse was turned on for 0.4 yr creating a second bubble, and then the jet inflow was turned off for 5.6 yr. Figure 12a depicts the flow after the two initial pulses. A third pulse was turned on for 0.4 yr, and the jet inflow was turned off for 5.6 yr; finally a fourth pulse was turned on for 0.4 yr, and then the jet inflow was turned off for 2.6 yr. Figure 12b depicts the flow after the fourth pulse. The third and fourth pulses create internal shocks *within* the bubbles that formed from the first and second bubbles. The third pulse has almost merged with the second pulse and the third pulse has just propagated into the first bubble at 24 yr.

These simulations produce limb-brightened bubbles and internal knots like those seen on the N side of the outflow from XZ Tau A, supporting the idea that a jet pulsed by strong velocity variations is the basic underlying mechanism of the flow. The diameter of the simulated bubbles agrees with the Hubble images: roughly 6×10^{10} km ($\sim 3''$). A wide-angle wind is not necessary to

Table 8. Outflow Simulation Parameters

Parameter	Units	Jet	Ambient
Gas density	H atoms cm^{-3}	500	50
Gas velocity	km s^{-1}	200	0
Gas temperature	K	1000	10000
Sound speed	km s^{-1}	3.8	12

match the morphology of the imaged flows. Several model details remain unoptimized, however: the initially static ambient medium makes the shock in the outer bubble stronger and less spherically symmetric than seen in XZ Tau; the jet width in the simulations is oversized compared to the knots observed in the HST images; and we do not yet have specific predictions for the optical emission line fluxes.

6. Summary

Our multiepoch *HST* observations of the young XZ Tau binary reveal a more complex system of outflows than was previously suspected. Both stars have collimated, bipolar jets as shown by the motions of compact knots. The knots in the XZ Tau A jet, which is oriented along $\text{PA}=15^\circ$, have tangential velocities of $80 - 200 \text{ km sec}^{-1}$. This jet is assumed to be inclined by $\sim 27^\circ$ from the plane of the sky. It can be traced to $19''$ to the south where it apparently impacts the edge of an interstellar cloud, creating a broad shock ($\text{H}\alpha\text{-A}$) that travels at 100 km sec^{-1} . The XZ Tau A jet knots show a surprising variety of forms, including fans, bow shocks, and shells, some of which suddenly appear and then fade away with a year or two. The more sedate XZ Tau B jet is defined by a pair of knots aligned along $\text{PA}=36^\circ$ with velocities of $40 - 125 \text{ km sec}^{-1}$. Although XZ Tau B is more photometrically variable and has richer spectral features than XZ Tau A, it is not the primary outflow driver as was previously assumed.

The most unusual aspect of the XZ Tau outflow is the series of bipolar bubbles that are aligned with the XZ Tau A jet. The outermost bubble in the northern outflow extended to $6''.1$ from the star and was $4''.5$ wide in early 2005. The tangential velocity of its forward edge was $\sim 130 \text{ km sec}^{-1}$ prior to 1999, and it slowed to $\sim 93 \text{ km sec}^{-1}$ by 2002, presumably due to interaction with the surrounding medium. At later epochs the outer edge became deformed and fragmented. Its transverse velocity of $46 - 76 \text{ km sec}^{-1}$ is probably indicative of the true expansion velocity from its center, which by derivation has a forward velocity of $\sim 65 \text{ km sec}^{-1}$ along the jet. The bubble was dominated by interior emission in 1995, but in later epochs it appeared limb brightened due to cooling and the resulting recombination emission. The northern extension of the XZ Tau A jet appears to terminate at the forward edge of the bubble where it brightens due to the impact with the same ISM material that is slowing the bubble.

Two additional bubbles trail the outer one and appear to overlap it. The one closest to the stars appears as a nearly circular shell with strong limb brightening, while the intermediate bubble is fainter with strong brightening along its forward edge. Another, more circular and more uniformly illuminated bubble appears on the southern side of the stars in the 2004 ACS images.

The bubbles do not appear similar to the typical bow shocks seen in the jets of other young stars and must have a different origin. Notably, the outer bubble was a filled volume of emitting gas in 1995, not a limb-brightened bow shock. The form and expansion velocity of the outer bubble suggests that it may have been created by a very hot and dense shock generated close to the star.

The shock may have rapidly expanded until it transitioned to a ballistically expanding bubble. Recombination within the cooling interior would cause the emission seen in 1995. Density enhancement along the outer boundary may have accelerated the cooling, creating additional emission seen along the limb after then. Additional interactions of the XZ Tau A jet with the bubble material may have created the trailing bubbles. The southern bubble may have formed at the same time in a bipolar outburst, but because of a possibly less-dense external medium it appears more uniform.

XZ Tau presents a unique collection of unusual outflow phenomena that vary considerably on timescales and distances that can be observed using the capabilities of *HST*. It represents a test of the ability of current methods of jet modeling.

7. Acknowledgements

This research has made use of the Hubble Space Telescope, operated by the Space Telescope Science Institute under a contract with NASA. This research was supported by *HST* GO grants 6754, 8289, 8771, 9236, and 9863 to STScI, Arizona State University, and to the Jet Propulsion Laboratory, California Institute of Technology. We would like to thank Angela Cotera for allowing us the use of her ACS polarimetric images for this study and Andrew Williams for assembling the animated version of Figure 12.

8. References

REFERENCES

- Bonnell, I., & Bastien, P. 1992, *ApJ*, 401, L31
- Brown, A., Drake, S. A., & Mundt, R. 1985, *Radio Stars*, 116, 105
- Burrows, C. J., et al. 1996, *ApJ*, 473, 437
- Carkner, L., Feigelson, E. D., Koyama, K., Montmerle, T., & Reid, I. N. 1996, *ApJ*, 464, 286
- Coffey, D., Downes, T. P., & Ray, T. P. 2004, *A&A*, 419, 593
- Giardino, G., Favata, F., Silva, B., Micela, G., Reale, F., & Sciortino, S. 2006, *A&A*, 453, 241
- Gilliland, R. L. 2004, ACS Instrument Science Report 04-01 (Baltimore:STScI)
- Ha, Y., Gardner, C. L., Gelb, A., and Shu, C.-W. 2005, *Journal of Scientific Computing*, 24, 29
- Hartigan, P., Kenyon, S.J. 2003, *ApJ*, 583, 334
- Hester, J.J., Stapelfeldt, K.R., Scowen, P.A. 1998, *AJ*, 116, 372

- Hirth, G. A., Mundt, R., & Solf, J. 1997, *A&AS*, 126, 437
- König, B., Neuhäuser, R., & Stelzer, B. 2001, *A&A*, 369, 971
- Krist, J. E., & Burrows, C. J. 1995, *Appl. Opt.*, 34, 4951
- Krist, J. E., & Hook, R. N. 1997, *The 1997 HST Calibration Workshop with a New Generation of Instruments*, p. 192, 192
- Krist, J. E., et al. 1997, *ApJ*, 481, 447
- Krist, J. E., et al. 1999, *ApJ*, 515, L35
- Moriarty-Schieven, G.H., Johnstone, D., Bally, J., Jenness, T. 2006, *ApJ*, 645, 357
- Movsessian, T.A., Magakian, T.Yu., Bally, J., Smith, M.D., Moiseev, A.V., Dodonov, S.N. 2007, *A&A*, 470, 605
- Mundt, R., Buehrke, T., Solf, J., Ray, T. P., & Raga, A. C. 1990, *A&A*, 232, 37
- Pavlovsky, C., et al. 2004, *ACS Data Handbook* (Baltimore:STScI)
- Reipurth, B., Heathcote, S., Morse, J., Hartigan, P., & Bally, J. 2002, *AJ*, 123, 362
- Reipurth, B., & Bally, J. 2001, *ARA&A*, 39, 403
- Rodriguez, L. F., Canto, J., Torrelles, J. M., Gomez, J. F., Anglada, G., & Ho, P. T. P. 1994, *ApJ*, 427, L103
- Schmutzler, T., & Tscharnuter, W. M. 1993, *A&A*, 273, 318
- Shu, C.-W. 1999, in *High-Order Methods for Computational Physics*, *Lecture Notes in Computational Science and Engineering*, 9, 439. New York: Springer Verlag
- Solf, J., Böhm, K.-H., Raga, A. 1988, *ApJ*, 334, 229
- Stapelfeldt, K.R. et al. 1995, *ApJ*, 449, 888
- Watson, A.M., Stapelfeldt, K.R. 2007, *AJ*, 133, 845
- Welch, W. J., Hartmann, L., Helfer, T., & Briceño, C. 2000, *ApJ*, 540, 362
- White, R. J., & Ghez, A. M. 2001, *ApJ*, 556, 265

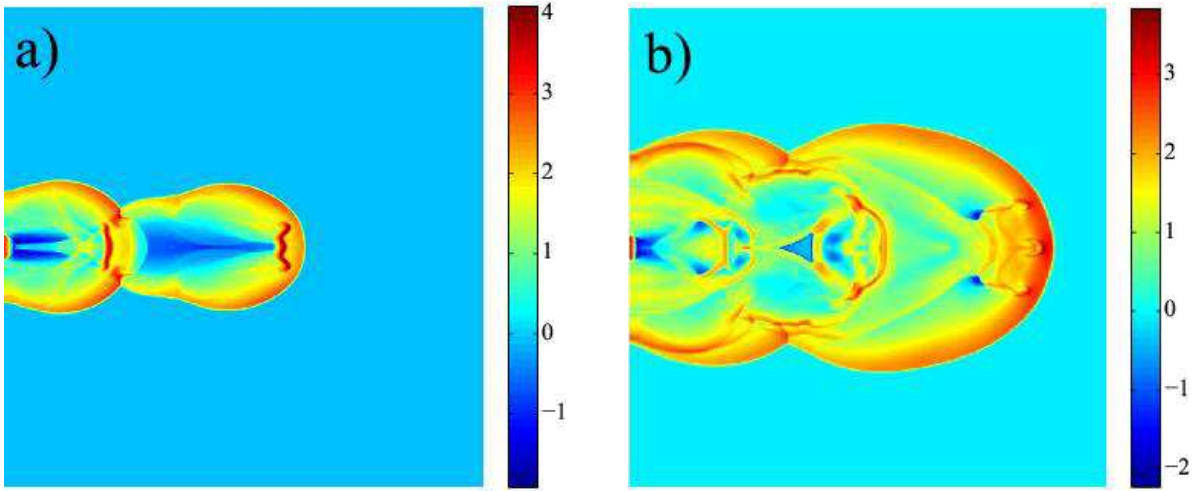


Fig. 12.— Radiative cooling $\log_{10}\{n^2\Lambda(T)/\bar{C}\}$ of the jet, where $\bar{C} = 1.044 \times 10^{-8} \text{ eV}/(\text{cm}^3 \text{ s}) \equiv 1.2115 \times 10^{-4} \text{ K}/(\text{cm}^3 \text{ s})$, shown for simulated flow ages of (a) 15 and (b) 24 yrs. The simulation regions are 10^{11} km on a side. An animated sequence of these and other epochs spanning 9–24 yr is available online via the *Astronomical Journal*.